# Large exchange bias in Mn-Ni-Sn Heusler alloys: Role of cluster spin glass state

Jyoti Sharma,[1] K. G. Suresh,[2] and Aftab Alam[1,*]

[1]*Materials Modeling Laboratory, Department of Physics, Indian Institute of Technology Bombay, Mumbai, 400076 India*

[2]*Magnetic Materials Laboratory, Department of Physics, Indian Institute of Technology Bombay, Mumbai, 400076 India*

(Received 11 October 2022; accepted 23 January 2023; published 7 February 2023)

We report a combined experimental and theoretical study of the exchange bias (EB), structural and magnetic properties of manganese-rich $Mn_{50}Ni_{41.5+x}Sn_{8.5-x}$ ($x = 0, 0.75$, and 1) Heusler alloys. All these alloys crystallize in a tetragonal structure at room temperature. *Ab initio* simulation using density functional theory (DFT) on off-stoichiometric $Mn_{50}Ni_{42.1875}Sn_{7.8125}$ alloy (very close to the actual composition) predicts the tetragonal structure with the ferrimagnetic arrangement as the ground state, in good agreement with the experimental results. These alloys are found to exhibit a large exchange bias at low temperatures, with a maximum EB field of 7.1 kOe at 2 K for $x = 1$, which is significantly larger than that reported for any Mn-Ni–based Heusler systems. Frequency dependence of spin freezing temperature obeying the scaling law confirms the presence of a cluster spin glass (CSG)–like state in these alloys. The latter is also confirmed from the memory and aging effect studies in zero-field cooling and field-cooled protocols for these alloys. The large EB is attributed to the strong exchange coupling between the CSG clusters embedded in an otherwise ferrimagnetic matrix. The exchange mechanism behind the large EB effect is discussed in the light of varying bond lengths between different magnetic pairs, and hence the magnetic coupling, due to the large tetragonal distortion. The present experimental findings are found to be in good agreement with the DFT results.

DOI: 10.1103/PhysRevB.107.054405

## I. INTRODUCTION

Generally, the exchange bias (EB) effect is observed in materials having different kinds of interfaces such as ferromagnetic (FM)/antiferromagnetic (AFM), spin glass (SG)/FM, SG/ferrimagnetic (FI), or FM/FI [1–4]. EB is manifested by the shifting of the magnetic hysteresis ($M$-$H$) loop with respect to the magnetic field axis, when material is field-cooled to low temperatures, from well above the critical transition temperatures of AFM/FM phases; this is termed conventional EB [1,5]. EB has attracted much attention due to its potential applications such as in spintronics, magnetic data storage, and sensing devices [6,7]. In addition to its application potential, the origin of the EB effect is still a subject of fundamental interest and debate. In the last few decades, nickel-rich Ni-Mn-$Z$ ($Z$ = Ga, Sb, Sn, and In) Heusler alloys have attracted a great deal of attention because of their multifunctional properties such as shape memory effect, large magnetocaloric effect, giant magnetoresistance, exchange bias, etc., most of which are attributed to their first-order magnetostructural (i.e., martensitic) transition, which occurs from a high-temperature austenite phase to a low-temperature martensite phase [8–11]. In these alloys, the magnetic state of the austenite phase is usually ferromagnetic in nature, whereas that of the martensite phase is generally found to be complex and often has coexisting AFM, FI, reentrant SG, or cluster SG (CSG), depending upon the interplay between the different kinds of exchange interactions present in the material [12–16]. It has been seen that the magnetic properties of these Ni-Mn-based Heusler alloys can be easily tuned by simply changing the composition, and thereby the exchange interactions, which are strongly sensitive to the Mn-Mn interatomic distances. As magnetic properties of these alloys are mainly governed by the manganese magnetic moments, Mn-Mn AFM/FM exchange interactions are expected to be stronger in the manganese-rich (Mn $\sim$ 50 at.%) Mn-Ni-Z alloys than in nickel-rich (Ni $\sim$ 50 at.%) Ni-Mn-$Z$ alloys. In the last few years, particularly some manganese-rich–based tetragonally distorted Heusler alloys have attracted immense attention in the research community due to the existence of compensated FI behavior, noncolinear magnetism, high ordering temperatures, high spin polarization, etc., owing to the large magnetocrystalline anisotropy created by the tetragonal distortion, which is a requirement of modern storage technologies such as in spin-transfer torque magneto resistive random access memory (STT-MRRAM) [17,18]. Therefore, it is interesting to explore some new tetragonal manganese-rich Heusler alloys from fundamental as well as application points of view, such as in high-density magnetic recording media and STT-MRRAM devices.

Conventional EB has been studied in many off-stoichiometric Ni-Mn-$Z$ Heusler alloys. For example, in Ni-Mn-Sn alloys, an EB field ($H_{EB}$) of 377 Oe was observed [19], whereas the $Ni_{50}Mn_{25+x}Sb_{25-x}$ and $Ni_{50}Mn_{50-x}In_x$ Heusler alloys have been found to show $H_{EB}$ values of 248 Oe and 120 Oe, respectively [11,20]. In contrast to nickel-rich alloys, Ma *et al.* [21] have reported a larger $H_{EB}$ of 1170 Oe in manganese-rich $Mn_2Ni_{1.6}Sn_{0.4}$, and an $H_{EB}$ of 16 mT has been observed in $Mn_2PtIn$ [22]. To date, only a few Mn-Ni–based Heusler alloys along with large tetragonal distortion have been explored for their exchange bias

*aftab@iitb.ac.in

 

properties. In one of our previous works [23], we reported a maximum EB field of 3.5 kOe in similar Mn-Ni–based Heusler alloys. In the current work, however, we report a giant EB effect in manganese-rich $Mn_{50}Ni_{41.5+x}Sn_{8.5-x}$ alloys for $x = 0$, 0.75, and 1. It is worth noting that these compounds are often sensitive to small changes in their compositions (as demonstrated in various earlier reports [24]). This is precisely being utilized to achieve such a high EB field in the present set of off-stoichiometric Mn-Ni alloys. Understanding the fundamental origin behind such enhanced EB is crucial. Heusler alloys have a special advantage because of their reasonably large magnetocrystalline anisotropy, mediated by tetragonal distortion. In order to understand the microscopic origin behind this enhanced EB field, we have performed first-principles simulations to study the structure, ground-state magnetic ordering, and the exchange mechanism for the measured alloys. A unique ferrimagnetic ordering turns out to be, energetically, the most favorable state, with two manganese atoms (on two different sublattices) coupled antiferromagnetically, while the manganese and nickel atoms coupled ferromagnetically in the stoichiometric $Mn_2NiSn$ alloy. In the off-stoichiometric $Mn_{50}Ni_{41.5+x}Sn_{8.5-x}$ alloy, the bond lengths between each pair decreases due to strong tetragonal distortion, making the AFM coupling much stronger. Interestingly, this decrease in bond lengths causes Mn-Ni pairs to align antiferromagnetically, while other Mn-Mn pairs retain their alignment—a plausible reason for the enhanced EB.

## II. EXPERIMENTAL DETAILS

Polycrystalline samples of $Mn_{50}Ni_{41.5+x}Sn_{8.5-x}$ ($x = 0$, 0.75, and 1) were prepared by the arc-melting method in the presence of a highly pure argon atmosphere, and were subsequently annealed at 1073 K for 70 h, followed by quenching in liquid nitrogen. The energy dispersive x-ray (EDX) spectroscopy (along with scanning electron microscopy) measurements showed the actual compositions of present alloys such as $Mn_{49.53}Ni_{42.02}Sn_{8.45}$, $Mn_{50.14}Ni_{42.13}Sn_{7.73}$, and $Mn_{49.34}Ni_{43.22}Sn_{7.44}$ for $x = 0$, 0.75, and 1, respectively. Structural analysis was performed by collecting the room-temperature (RT) X-ray diffraction (XRD) patterns using the PANalytical X'pert PRO diffractometer. The data are shown in Supplemental Material Fig. S1 [25]. The Le Bail refinement using FullProf suite confirms that all the alloys possess a tetragonal structure at RT with a change in lattice parameters (as mentioned in the first para of XRD section of Supplemental Material [25]). The $c/a$ ratio is found to increase with an increase in nickel content ($x$), which indicates the increase in the tetragonal distortion in the alloys. This indicates that the occurrence of the martensitic transition is expected to be above RT in these alloys. DC magnetization as a function of temperature ($M$-$T$), magnetic field ($M$ vs. $H$), and frequency-dependent AC susceptibility ($\chi$) measurements was performed using a superconducting quantum interference device magnetometer.

### Computational details

First-principles calculations were performed using the Vienna *Ab initio* Simulation Package within the projected augmented wave formalism with an energy cutoff of 350 eV. Generalized-gradient approximation by Perdew-Burke-Ernzerhof was used to describe the exchange and correlation. Total energy (force) is converged up to $10^{-6}$ eV/cell (0.01 eV/Å). First, we simulated a conventional unit cell (16 atoms) of a $Mn_2NiSn$ (stoichiometric) Heusler alloy using the Γ-centered $K$-mesh of $8 \times 8 \times 8$ points for Brillouin zone (BZ) integration. After that, a $2 \times 2 \times 2$ supercell (128 atoms) of the conventional cell was used to simulate $Mn_{50}Ni_{42.1875}Sn_{7.8125}$ (close to the actual alloy composition), where $6 \times 6 \times 6$ $K$-mesh is used for BZ integration.

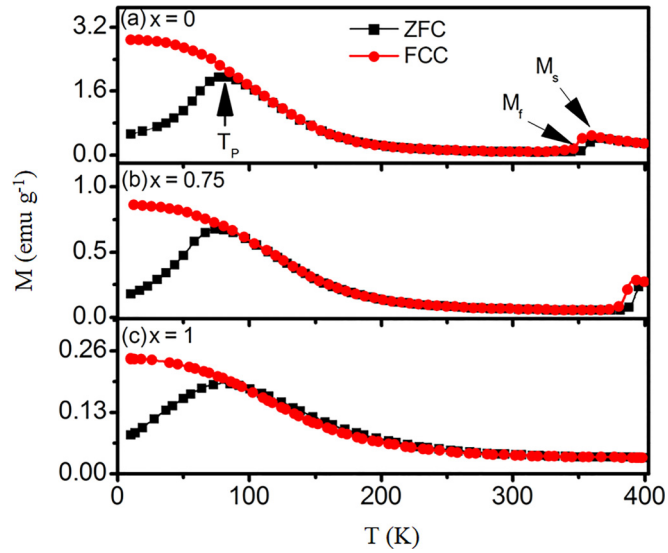


FIG. 1. ZFC and FCC $M$-$T$ curves for (a) $x = 0$, (b) $x = 0.75$, and (c) $x = 1$ of $Mn_{50}Ni_{41.5+x}Sn_{8.5-x}$ alloys.

## III. RESULTS AND DISCUSSION

Figure 1 shows zero-field cooling (ZFC) and field-cooled cooling (FCC) magnetization vs. temperature ($M$-$T$) curves for $Mn_{50}Ni_{41.5+x}Sn_{8.5-x}$ ($x = 0$, 0.75, and 1) alloys, measured in a 1 kOe field. For $x = 0$, a sudden jump in magnetization is observed at around 356 K, which corresponds to the martensite start temperature ($M_S$), and attains minimum magnetization at 345 K, which corresponds to the martensite finish temperature ($M_f$). Below $M_f$, with lowering the temperature, the ZFC and FCC curves start to split at around 120 K, and a peak was observed at 78 K (marked as $T_P$) in the ZFC $M$-$T$ curve. With a further decrease in temperature, the splitting becomes more pronounced, which indicates the coexistence of magnetically inhomogeneous phases such as AFM/FM or spin glass/FM or FI in the martensite phase of these alloys. [13,14,18,22]. However, it can be seen that with the increase in $x$, the martensitic transition temperature increases, as for $x = 0.75$, $M_s$ and $M_f$ are 391 and 381 K, respectively, while no martensitic transition is observed for composition $x = 1$ up to 400 K (our instrument measurement limit). This increase in martensitic transition temperature is attributed to the increase in the valence electron concentration (e/$a$ ratio) with $x$; as for $x = 0$, e/$a = 7.99$, while it becomes 8.05 for $x = 1$, which matches well with the trend observed in other Ni-Mn-Z Heusler alloys [16,26]. Relatively low magnetization values

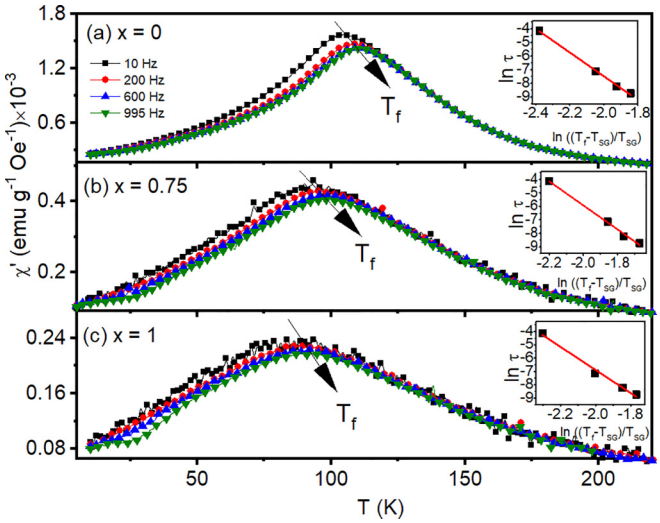


FIG. 2. Temperature dependence of the real part of AC susceptibility ($\chi'$) at different frequencies for (a) $x = 0$, (b) $x = 0.75$, and (c) $x = 1$. Insets show the variation of $\ln\tau$ with $\ln[(T_f–T_{SG})/T_{SG}]$. The solid line represents the linear fit to the scaling law.

observed in the present alloys suggest ferrimagnetic ordering, as also seen in some other manganese-rich Heusler alloys [18,22]. The broadness of the transition is indicative of the slow relaxation of magnetic moments, as generally observed in SG systems [27,28].

In order to investigate the nature of the complex magnetic ground state of these alloys, AC susceptibility measurements have been performed at different frequencies. Figure 2 shows the real part of AC susceptibility as a function of temperature ($\chi'–T$), recorded at different frequencies ($f$) ranging from 10 to 995 Hz. For $x = 0$ [Fig. 2(a)], a peak is observed in $\chi'–T$ curves at around 105 K at 10 Hz, which is found to shift to higher temperatures with increasing frequency, indicating the presence of the SG state [27,28]. This peak is defined as the spin freezing temperature ($T_f$). However, $T_f$ is found to decrease with an increase in $x$, as $T_f$ becomes 86 K at 10 Hz for $x = 1$. The decrease in $T_f$ with $x$ is in agreement with the trend observed for the peak in DC $M$-$T$ curves (Fig. 1). The shift of $T_f$ with frequency in $\chi'$-$T$ curves (known as the Mydosh parameter) is quantified using the relation [29]

$$\delta T_f = \Delta T_f/(T_f \Delta \log \omega),$$

where $\Delta T_f$ is maximum change in $T_f$, and $\omega$ is the angular frequency of the AC excitation. Estimated values of $\Delta T_f$ are 0.035, 0.030, and 0.032 for $x = 0$, 0.75, and 1, respectively, which are comparable to those reported for many CSG systems, and much smaller than the typical value of around 0.1 for the superparamagnetic (SPM) state [28–31]. In order to investigate the CSG state further, present results have been analyzed using the dynamic scaling law

$$\tau = \tau_0(T_f/T_{SG} - 1)^{-z\nu},$$

where $\tau_0$, $T_{SG}$, $z$, and $\nu$ are microscopic relaxation time, spin glass transition temperature, dynamical critical exponent, and spin correlation length exponent, respectively [30,31]. Plots between $\ln\tau$ and $\ln[(T_f–T_{SG})/T_{SG}]$ for each composition are shown in the insets of Fig. 2. The $T_{SG}$ values are found to be 96 K, 84 K, and 78 K for $x = 0$, 0.75, and 1, respectively, from the fitted curves. The obtained values of $\tau_0$ are $1.02 \times 10^{-11}$ ($z\nu = 9.1$), $5.09 \times 10^{-11}$ ($z\nu = 8.9$), and $3.09 \times 10^{-11}$ ($z\nu = 8.6$) for $x = 0$, 0.75, and 1, respectively. These fitted parameters match well with those reported for other CSG systems, such as $\tau_0 \sim 10^{-12}$ ($z\nu = 9.7$) for Ni-Co-Mn-Sn, $\tau_0 \sim 10^{-11}$ ($z\nu = 7.3$) in $CeNi_{0.5}Cu_{0.5}$, $\tau_0 \sim 10^{-12}$ ($z\nu = 8$) in core-shell NiO nanoparticles, and $\tau_0 \sim 10^{-10}$ ($z\nu = 10.3$) for $La_{0.95}Sr_{0.05}CoO_3$ [28,32–34]. These larger values of $\tau_0$, unlike the ones observed in canonical SG systems, indicate the slower dynamics of SG clusters, which may be due to the fact that the dominant interactions are among clusters, rather than among individual spin magnetic moments. The collected AC susceptibility data have also been fitted to the Neel-Arrhenius law, which holds for noninteracting SPM-type clusters:

$$\tau = \tau_0 \exp(E_a/k_B T_f),$$

where $E_a$ is the anisotropy energy barrier and $k_B$ is the Boltzmann constant [31]. The fitted curves are shown in Supplemental Material Fig. S2 [25]. The value of $E_a$ is found to be on the order of $\sim 10^{-23}$ J, and unphysically small values of $\tau_0 \sim 10^{-38}$ s, $10^{-34}$ s and $10^{-37}$ s are obtained for $x = 0$, 0.75, and 1, respectively, which rules out any possibility of an SPM-like state in these alloys.

To shed more light onto the presence of the CSG-like state and to understand the dynamics of SG clusters, the memory and aging effect (i.e., the characteristics of a SG) related experiments have also been carried out in ZFC and field-cooled (FC) protocols. For the memory effect, with the ZFC stop-and-wait protocol, the sample was first cooled to 5 K in the absence of field, and then $M$-$T$ curves were recorded in the presence of 500 Oe (the reference curve). Subsequently, the stop-and-wait procedure was applied, in which the sample was initially cooled to an intermediate stop temperature ($< T_f$ as typically 50 K and 60 K are taken for $x = 0$ and 1, respectively), and then waited there for $10^3$ s, before cooling to 5 K. Subsequently, $M$-$T$ curves were again recorded in the presence of the same field, called the stop-and-wait curve. Figure 3(a) and (b) shows the reference and stop-and-wait $M$-$T$ curves, and insets show the temperature dependence of the magnetization difference between the stop-and-wait and the reference $M$-$T$ curves. It can be seen from the figure that significant magnetization dips were observed at 50 K and 60 K for $x = 0$ and 1, respectively, which confirm the presence of a memory effect in these alloys, revealing the existence of the CSG state [35,36].

Furthermore, for the aging effect with the ZFC aging protocol, the sample was cooled in the absence of field to an intermediate stop temperature [such as a typical case of 60 K (i.e., below $T_f$) for $x = 1$], and waited there for a period of time ($t_w$). Subsequently, magnetization was recorded as a function of time ($t$) in presence of 500 Oe [37]. The $M$-$t$ curves reordered with this protocol for different time durations such as $t_w = 500$ s, 3000 s, and 8000 s for $x = 1$ are shown in Supplemental Fig. S3 [25], and shows a strong magnetization dependence on $t_w$ and confirms the presence of an aging effect in these alloys. It is to be noted that magnetization does not saturate even after 2.2 h (measurement time), which is attributed to the fact that in the CSG state, moments are

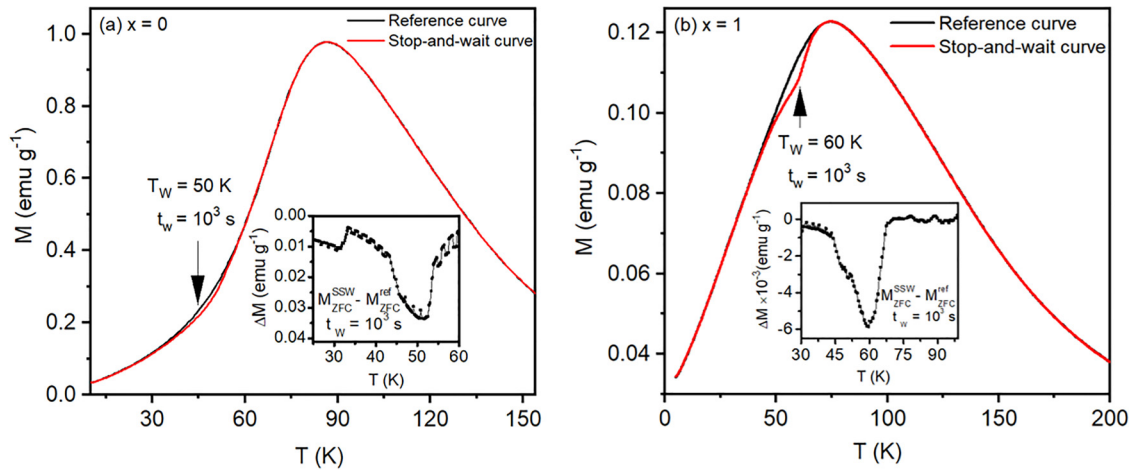


FIG. 3. Memory effect: Temperature dependence of ZFC magnetization, with and without the stop-and-wait protocol, measured at 500 Oe for (a) $x = 0$ and (b) $x = 1$. Insets show the temperature dependence of difference between magnetization of stop-and-wait and reference $M$-$T$ curves.

randomly frozen along their anisotropy axes, and it takes a long time to align them along the field direction. The same measurement was repeated with the FC aging protocol, in which the sample was first cooled from 300 K to 60 K in the presence of 500 Oe, followed by waiting there for a time period of $t_w$, then magnetization was recorded as a function of time by switching off the field. FC aging protocol $M$-$t$ curves for $x = 1$, recorded for $t_w = 3000$ s and 8000 s, are shown in inset of Supplemental Material Fig. S3 [25]. A strong dependence of waiting time on the magnetization with the FC aging protocol again confirms the slow dynamics of CSG clusters, unlike in canonical SG. According to the Fisher and Huse droplet model, a CSG state remains unperturbed at an intermediate stop temperature (below $T_f$) for time period $t_w$, followed by its quenching from the temperature above $T_f$ [38,39]. At that intermediate stop temperature, spin configuration gets rearranged within the clusters via a slow process, which leads to an increase in cluster domain size and results in a reduction of domain wall energy. This explains the mechanism responsible for the dependence of CSG-phase collective magnetization dynamics on waiting time, which causes aging. Therefore, the memory and aging measurements strongly confirm the CSG-like state at low temperatures in the present alloys.

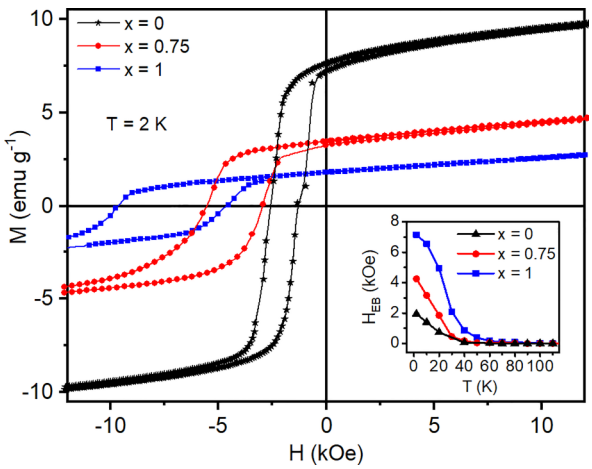


FIG. 4. Magnetic hysteresis loops measured at 2 K after FC at 10 kOe. Variation of $H_{EB}$ as a function of temperature for the studied alloys.

Generally, it is seen that the magnetic frustration leads to the EB effect. Therefore, to study the EB effect in present alloys, we have recorded the magnetic hysteresis ($M$-$H$) loops at 2 K in the field range of ±20 kOe, after field cooling at 10 kOe, and the data are shown in Fig. 4 (in the range of ±12 kOe for better clarity). It can be seen in Fig. 4 that all magnetic hysteresis ($M$-$H$) loops shift toward the negative field axis, which confirms the presence of EB. The values of the $H_{EB}$ and the coercive field ($H_C$) were calculated by using formulae $H_{EB} = -(H + H_R)/2$ and $H_C = |H_L - H_R|/2$, respectively, where $H_L$ and $H_R$ are the left and right cutoff fields, respectively. The estimated values are listed in Table I. With the increase of $x$, both $H_{EB}$ and $H_C$ increase, as $H_{EB}$ is around 1.9 kOe for $x = 0$, and increase to 7.1 kOe for $x = 1$. The observed maximum value of EB in the present alloys have not been reported so far in any other Mn-Ni–based Heusler alloys, and also were found to be significantly larger than reported for many other systems in the literature [11,15,19,21,22]. To verify the EB effect further, magnetic hysteresis ($M$-$H$) loops were also recorded at 2 K in the same field range after FC at −10 kOe, and a typical case for $x = 1$ is shown in Supplemental Material Fig. S4 [25]. The magnetic hysteresis ($M$-$H$) loop gets shifted toward the positive field direction, with a nearly similar value of $H_{EB}$, obtained for FC at +10 kOe.

TABLE I. The estimated values of $H_{EB}$ and $H_C$ for various $x$ of $Mn_{50}Ni_{41.5+x}Sn_{8.5-x}$ alloys.

| Composition ($x$) | $H_{EB}$(kOe) | $H_C$(kOe) |
|---|---|---|
| 0 | 1.9 | 0.6 |
| 0.75 | 4.3 | 1.3 |
| 1 | 7.1 | 2.5 |

TABLE II. The calculated lattice parameter ($a_0$), total magnetic moment ($\mu_{tot}$), atom-projected moments ($\mu_i$), and relative energies ($\Delta E_{Total}$) of nonmagnetic (NM), ferromagnetic (FM), and ferrimagnetic (FI) states of the stoichiometric $Mn_2NiSn$ Heusler alloy. FI is taken as the reference state with energy 0 eV/f.u.

| Magnetic Config. | $a_0$ (Å) | $\mu_{tot}$ ($\mu_B$ f.u.$^{-1}$) | $\mu_{MnI}$ ($\mu_B$) | $\mu_{MnII}$ ($\mu_B$) | $\mu_{Ni}$ ($\mu_B$) | $\mu_{Sn}$ ($\mu_B$) | $\Delta E_{Total}$ (eV f.u.$^{-1}$) | Ref. |
|---|---|---|---|---|---|---|---|---|
| NM | 5.93 | | | | | | 4.61 | Present work |
| FM | 6.03 | 15.60 | 3.06 | 0.45 | 0.44 | –0.05 | 1.38 | |
| FI | 6.13 | 2.76 | 3.76 | –2.95 | –0.11 | –0.01 | 0 | |
| FI (expt1) | | 2.48 | 4.49 | –2.01 | | | | 38 |
| FI (expt2) | 6.02 | 2.95 | | | | | | 39 |
| FI (theory) | 6.149 | 0.55 | 3.69 | –3.29 | 0.12 | 0.03 | | 40 |

The origin of magnetic clusters comprising the CSG phase in these alloys may be attributed to the presence of chemical and/or structural inhomogeneities. The latter may include the atomic disorder (i.e., occupancies of different sites in the lattice) and compositional disorder at the local level. Generally, in the manganese-rich Mn-Ni-Z Heusler alloys, excess manganese atoms have been observed to occupy both $Z$ and nickel sites, which couple antiferromagnetically with the regular manganese atoms [21]. Apart from that, the martensitic transition also leads to the shrinking of crystallographic axes due to the twining of martensite variants, which results in the further decrease of the Mn-Mn distance, thereby leading to the enhanced AFM coupling in these alloys. We have also estimated the nearest neighbor distances between regular manganese and manganese atoms at tin and nickel sites using lattice parameters (discussed in the first para of XRD section of Supplemental Material [25]), which indicates the presence of AFM coupling between them, due to a distance of less than 3 Å. In fact, with the increase in $x$, these distances are found to decrease further due to the increase in tetragonal distortion ($c/a$ ratio), which suggests the further enhancement of AFM coupling, and results in large exchange anisotropy at the interfaces. This may be due to the larger atomic radii of tin compared to nickel atoms. Thus, due to the random distribution of excess manganese atoms at tin and nickel sites in the present alloys, it is expected that disordered Mn-Mn clusters have been formed in the martensite phase. They are maintained up to low temperatures, and freeze below $T_f$, which gives rise to the CSG state. Therefore, the CSG phase (i.e., comprised of Mn-Mn disordered clusters) embedded in a FI matrix is expected to give rise to the strong exchange anisotropy at CSG/FI interfaces, resulting in a giant exchange bias in these alloys.

The effect of temperature on EB is also studied for these alloys. For that, magnetic hysteresis ($M$-$H$) loops were recorded at different temperatures, after FC at 10 kOe (data not shown). The variation of estimated $H_{EB}$ as a function of temperature is shown in the inset of Fig. 4. $H_{EB}$ is found to decrease monotonically with the increase in temperature and vanishes at around 60 K, 70 K, and 80 K for $x = 0$, 0.75, and 1, respectively, which are defined as the EB blocking temperatures ($T_B$), at which $H_{EB}$ vanishes. It can be seen that $T_B$ increases with increasing $x$ for these alloys, which also indicates the increase in exchange anisotropy with $x$. These alloys show reasonably large EB values up to 50 K. At low temperatures, interactions among the CSG clusters are strong enough to overcome the thermal energy, while with an increase in temperature, the interactions between them decrease due to the increase in thermal fluctuations, which leads to a weakening of exchange anisotropy. This results in a decrease of $H_{EB}$, and the observed trend matches well with other reported Heusler systems [18,21,22].

To complement the experimental results, we first theoretically calculated the ground-state properties of the stoichiometric $Mn_2NiSn$ alloy. The inverse Heusler structure ($Hg_2CuTi$ type, space group $F4$-$3m$) with different magnetic configurations is used to relax $Mn_2NiSn$ fully. In this structure, the energetically most favorable Wykoff positions

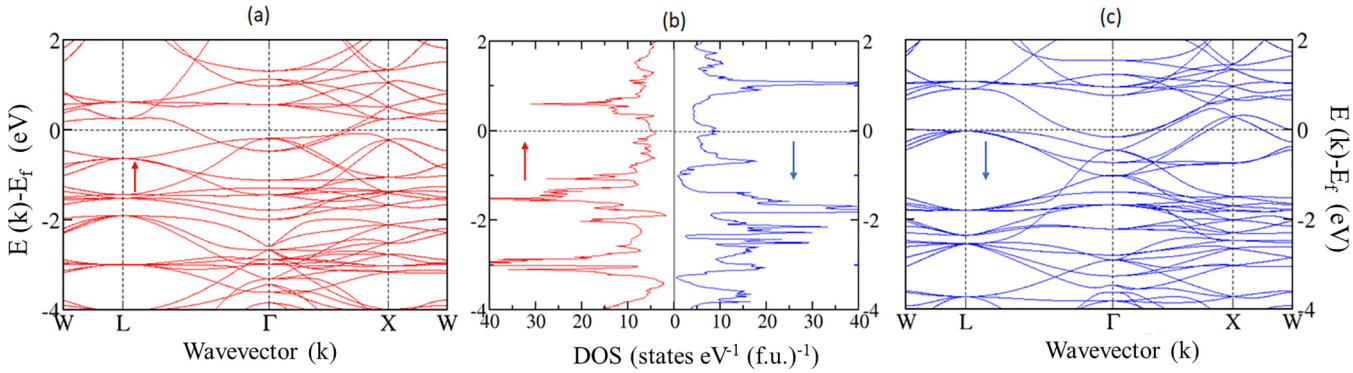


FIG. 5. Spin-resolved band structure for (a) spin up, (c) spin down, and (b) DOS [spin up (left) and spin down (right)] for the stoichiometric $Mn_2NiSn$ Heusler alloy in a FI configuration.

TABLE III. The calculated lattice parameters ($a_0$, $b_0$, $c_0$), total magnetic moment ($\mu_{tot}$), average atom projected moments ($\mu_i$), and relative energies ($\Delta E_{Total}$) of nonmagnetic, ferromagnetic, and ferrimagnetic state of off-stoichiometric $Mn_{50}Ni_{42.1875}Sn_{7.8125}$ alloy.

| Mag. Config. | $a_0$ (Å) | $b_0$ (Å) | $c_0$ (Å) | $\mu_{tot}$ ($\mu_B$ f.u.$^{-1}$) | $\mu_{MnI}$ ($\mu_B$) | $\mu_{MnII}$ ($\mu_B$) | $\mu_{Ni}$ ($\mu_B$) | $\mu_{Sn}$ ($\mu_B$) | $\Delta E_{Total}$ (eV f.u.$^{-1}$) |
|---|---|---|---|---|---|---|---|---|---|
| NM | 10.24 | 10.24 | 13.91 | | | | | | 3.44 |
| FM | 11.78 | 10.82 | 12.79 | 21.62 | 3.33 | 2.93 | 0.36 | –0.17 | 2.12 |
| FI | 10.38 | 10.38 | 14.81 | 0.94 | 3.03 | –3.10 | 0.04 | 0.05 | 0 |

of different atoms are as follows: $Mn_I$ at $4b(0.5, 0.5, 0.5)$, $Mn_{II}$ at $4c(0.25, 0.25, 0.25)$, tin at $4a(0, 0, 0)$ and nickel at $4d(0.75, 0.75, 0.75)$. Simulated relative energies, relaxed lattice parameters ($a_0$), total and atom-projected magnetic moments for nonmagnetic (NM), ferromagnetic, and ferrimagnetic ordering are listed in Table II. Clearly, the ferrimagnetic ordering is energetically the most stable magnetic configuration. Here, manganese atoms majorly contribute to the net magnetization (i.e., 2.76 $\mu_B$ f.u.$^{-1}$) of the alloy; however, the two manganese sites ($Mn_I$ and $Mn_{II}$) belonging to different sublattices are oppositely aligned, which partially compensates the moments and leads to the FI ordering. Our simulated total magnetic moment ($\mu_{tot}$) agrees fairly well with the experimentally reported value by neutron diffraction (see Table II) as well as with a few other simulated reports [40–42]. Figure 5 shows the spin-resolved band structure and density of states (DOS) of the stoichiometric $Mn_2NiSn$ alloy in the FI states, which clearly confirms the metallic character. It can be noticed from Fig. 5(b) that the DOS is split into bonding and antibonding states in both the spin channels. The FI ground state is also clearly evident from the exchange splitting between the two spin channels.

Next, we simulated a representative mixed-alloy composition ($Mn_{50}Ni_{42.1875}Sn_{7.8125}$) of our experimental off-stoichiometric case using a $2 \times 2 \times 2$ supercell. The structure was fully relaxed in different magnetic configurations. Simulated relative energies, relaxed lattice parameters ($a_0$, $b_0$, $c_0$), along with the total and atom-projected magnetic moments for the NM, FM, and FI states are listed in Table III. In this case also, FI is found to be energetically the most favorable magnetic ordering, but with a tetragonal structural distortion [$a_0 = b_0 = 10.38$ Å and $c_0 = 14.81$ Å (i.e., of supercell), $c_0/a_0 = 1.43$). The tetragonal distortion arises due to the off-stoichiometry, as also observed experimentally with a $c/a$ value of 1.35 for $x = 1$ composition. Figure 6 shows the spin-resolved DOS for $Mn_{50}Ni_{42.1875}Sn_{7.8125}$, which again confirms the metallic character. The FI ground state is clearly evident from the exchange splitting, as observed for the stoichiometric $Mn_2NiSn$ alloy.

To understand the exchange mechanism and the associated EB better in the present alloys, we have calculated the bond lengths between nearest neighbor manganese and other constituent atoms for stoichiometric $Mn_2NiSn$ as well as off-stoichiometric $Mn_{50}Ni_{42.1875}Sn_{7.8125}$ alloys. These are are listed in Table IV. As discussed earlier, in Mn-Ni-Sn–based Heusler alloys, the exchange interactions between the manganese moments are strongly influenced by the distance between them. If the interatomic distances are less than 3 Å, the coupling between them tends to be AFM. From Table IV, one can notice that $Mn_I$-$Mn_{II}$ atoms are the nearest neighbor pairs and the distance between them is 2.657 Å for $Mn_2NiSn$, which decreases significantly to 2.467 Å for $Mn_{50}Ni_{42.1875}Sn_{7.8125}$. This suggests that AFM coupling gets stronger in the off-stoichiometric alloys. In fact, the interatomic distances between other pairs, $Mn_I$-Sn and $Mn_{II}$-Ni, also decrease significantly in case of off-stoichiometric alloys compared to $Mn_2NiSn$, due to the enhanced tetragonal distortion. This causes a change in the magnetic coupling strength of FI in $Mn_2NiSn$ to FI in the $Mn_{50}Ni_{42.1875}Sn_{7.8125}$ alloy. However, manganese atoms at their regular sites couple ferromagnetically. This suggests that AFM coupling gets significantly enhanced in the off-stoichiometric $Mn_{50}Ni_{42.1875}Sn_{7.8125}$ alloy, resulting in a large exchange coupling at the CSG/FI interfaces and leads to the giant EB. The calculated interatomic distances are in good agreement with those estimated from the experimental lattice parameters (see the first para of XRD section of Supplemental Material [25]).

## IV. CONCLUSION

In conclusion, manganese-rich $Mn_{50}Ni_{41.5+x}Sn_{8.5-x}$ ($x = 0$, 0.75, and 1) Heusler alloys were synthesized by arc melting and found to possess a tetragonal structure at RT. DC magnetization measurements suggest that the martensitic transition occurs above RT for all compositions, and shows a large split between ZFC and FCC $M$-$T$ curves at low temperatures. Frequency-dependent AC susceptibility data obeying the scaling law along with memory and aging effects under various

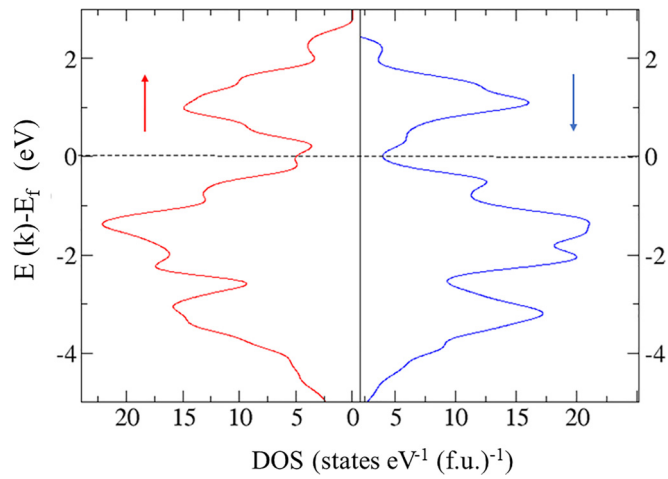


FIG. 6. Spin-resolved density of states [spin up (left) and spin down (right)] for the off-stoichiometric $Mn_{50}Ni_{42.1875}Sn_{7.8125}$ Heusler alloy in a FI configuration.

TABLE IV. Simulated bond lengths between different neighboring pairs of atoms for stoichiometric $Mn_2NiSn$ and off-stoichiometric $Mn_{50}Ni_{42.1875}Sn_{7.8125}$ alloys.

| Neighboring pairs | $Mn_2NiSn$ Bond length (Å) | $Mn_{50}Ni_{42.1875}Sn_{7.8125}$ Bond length (Å) |
|---|---|---|
| $Mn_{II}$-Ni | 3.068 | 2.479 |
| $Mn_I$-Ni | 2.657 | 2.597 |
| $Mn_{II}$-Sn | 2.657 | 2.763 |
| $Mn_I$-Sn | 3.068 | 2.597 |
| $Mn_{II}$-$Mn_I$ | 2.657 | 2.467 |

aging protocols confirm the cluster spin glass–like state at low temperatures. The present alloys have been found to show giant EB; a maximum $H_{EB}$ of 7.1 kOe is observed for $x = 1$, which is found to be significantly larger than that reported in any other Mn-Ni–based Heusler systems. The present values of EB are significantly larger than those reported in all previous studies, [19–22], including one of our earlier works [23], in a similar Mn-Ni–based Heusler alloy. These compounds are very sensitive to small changes in their compositions, as demonstrated in the present work [24]. First-principles density functional theory calculations were also carried out to verify and support the experimental findings further. For the stoichiometric $Mn_2NiSn$ alloy, an inverse Heusler structure with FI ordering is found to be energetically most favorable. On the other hand, the off-stoichiometric $Mn_{50}Ni_{42.1875}Sn_{7.8125}$ alloy (a representative case) also shows a tetragonal structural distortion with FI ordering to be energetically most stable, which is in good agreement with the experimental results. The calculated nearest neighbor bond lengths between manganese atoms at different sites suggest significant enhancement of AFM coupling in the off-stoichiometric alloys as a result of the enhanced tetragonal distortion. The calculated spin-resolved DOS and band structure suggest the metallic behavior for both the alloys. Strong exchange coupling between the CSG clusters embedded in a strong FI matrix is suggested to be responsible for the observed giant EB in these alloys. Thus current work not only represents the feasibility of achieving large perpendicular magnetic anisotropy along with the presence of a large exchange bias in these types of Heusler alloys, but also is a motivation to search for other Heusler alloys with even better properties for potential data storage and other spintronic applications.

## ACKNOWLEDGMENTS

J.S. thanks the Department of Science and Technology (DST) for financial support via the DST Women Scientist program (Grant No. DST/WOS-A/PM-77/2019). A.A. acknowledges DST-SERB (Grant No. CRG/2019/002050) for funding to support this research.

[1] S. Giri, M. Patra, and S. Majumdar, Exchange bias effect in alloys and compounds, J. Phys. Condens. Matter **23**, 073201 (2011).
[2] W. C. Cain and M. H. Kryder, Investigation of the exchange mechanism in NiFe-TbCo bilayers, J. Appl. Phys. **67**, 5722 (1990).
[3] W. A. Razzaq and J. S. Kouvel, Spin glassiness and ferromagnetism in disordered Ni-Mn, J. Appl. Phys. **55**, 1623 (1984).
[4] O. Iglesias, A. Labarta, and X. Batlle, Exchange bias phenomenology and models of core/shell nanoparticles, J. Nanosci. Nanotech. **8**, 2761 (2008).
[5] J. Nogues and I. K. Schuller, Exchange bias, J. Magn. Magn. Mater. **192**, 203 (1999).
[6] Y. T. Chen, S. U. Jen, Y. D. Yao, J. M. Wu, J. H. Liao, and T. B. Wu, Exchange biasing observed in the $Co/Ir_{20}Mn_{80}$ system, J. Alloys Compd. **448**, 59 (2008).
[7] I. L. Prejbeanu, M. Kerekes, R. C. Sousa, H. Sibuet, O. Redon, B. Dieny, and J. P. Nozières, Thermally assisted MRAM, J. Phys.: Condens. Matter **19**, 165218 (2007).
[8] K. Ullakko, J. K. Huang, C. Kantner, R. C. O'Handley, and V. V. Kokorin, Large magnetic-field-induced strains in $Ni_2MnGa$ single crystals, Appl. Phys. Lett. **69**, 1966 (1996).
[9] C. O. Aguilar-Ortiz, D. Soto-Parra, P. Alvarez-Alonso, P. Lazpita, D. Salazar, P. O. Castillo-Villa, H. Flores-Zúniga, and V. A. Chernenko, Influence of Fe doping and magnetic field on martensitic transition in Ni–Mn–Sn melt-spun ribbons, Acta Mater. **107**, 9 (2016).
[10] M. Pasquale, C. P. Sasso, L. H. Lewis, L. Giudici, and T. Lograsso, and D. Schlagel, Magnetostructural transition and magnetocaloric effect in $Ni_{55}Mn_{20}Ga_{25}$ single crystals, Phys. Rev. B **72**, 094435 (2005).
[11] M. Khan, I. Dubenko, S. Stadler, and N. Ali, Exchange bias behavior in Ni–Mn–Sb Heusler alloys, Appl. Phys. Lett. **91**, 072510 (2007).
[12] A. Planes, L. Mañosa, and M. Acet, Magnetocaloric effect and its relation to shape-memory properties in ferromagnetic Heusler alloys, J. Phys. Condens. Matter **21**, 233201 (2009).
[13] T. Kanomata, K. Fukushima, H. Nishihara, R. Kainuma, W. Itoh, K. Oikawa, K. Ishida, K. U. Neumann, and K. R. A. Ziebeck, Magnetic and crystallographic properties of shape memory alloys $Ni_2Mn_{1+x}Sn_{1-x}$, Mater. Sci. Forum **583**, 119 (2008).
[14] S. Chatterjee, S. Giri, S. K. De, and S. Majumdar, Reentrant-spin-glass state in $Ni_2Mn_{1.36}Sn_{0.64}$ shape-memory alloy, Phys. Rev. B **79**, 092410 (2009).
[15] A. K. Nayak, K. G. Suresh, and A. K. Nigam, Correlation between reentrant spin glass behavior and the magnetic order–disorder transition of the martensite phase in Ni–Co–Mn–Sb Heusler alloys, J. Phys. Condens. Matter **23**, 416004 (2011).
[16] Y. Sutou, Y. Imano, N. Koeda, T. Omori, R. Kainuma, K. Ishida, and K. Oikawa, Magnetic and martensitic transformations of NiMn$X$ ($X$ = In, Sn, Sb) ferromagnetic shape memory alloys, Appl. Phys. Lett. **85**, 4359 (2004).
[17] I. Galanakis, K. Ozdogan, E. Sasioglu, and B. Aktas, Doping of $Mn_2VAl$ and $Mn_2VSi$ Heusler alloys as a route to half-metallic antiferromagnetism, Phys. Rev. B **75**, 092407 (2007).
[18] A. K. Nayak, M. Nicklas, S. Chadov, P. Khuntia, C. Shekhar, A. Kalache, M. Baenitz, Y. Skourski, V. K. Guduru, A. Puri, U.

Zeitler, J. M. D. Coey, and C. Felser, Design of compensated ferrimagnetic Heusler alloys for giant tunable exchange bias, Nat. Mater. **14**, 679 (2015).

[19] S. E. Muthu, N. V. R. Rao, D. V. S. Rao, M. M. Raja, U. Devarajan, and S. Arumugam, Effect of Ni/Mn concentration on exchange bias properties in bulk $Ni_{50-x}Mn_{37+x}Sn_{13}$ Heusler alloys, J. Appl. Phys. **110**, 023904 (2011).

[20] A. K. Pathak, M. Khan, B. R. Gautam, S. Stadler, I. Dubenko, and N. Ali, Exchange bias in bulk Ni–Mn–In-based Heusler alloys, J. Magn. Magn. Mater. **321**, 963 (2009).

[21] L. Ma, W. H. Wang, J. B. Lu, J. Q. Li, C. M. Zhen, D. L. Hou, and G. H. Wu, Coexistence of reentrant-spin-glass and ferromagnetic martensitic phases in the $Mn_2Ni_{1.6}Sn_{0.4}$ Heusler alloy, Appl. Phys. Lett. **99**, 182507 (2011).

[22] A. K. Nayak, C. Shekhar, J. Winterlik, A. Gupta, and C. Felser, $Mn_2PtIn$: A tetragonal Heusler compound with exchange bias behavior, Appl. Phys. Lett. **100**, 152404 (2012).

[23] J. Sharma, and K. G. Suresh, Observation of giant exchange bias in bulk $Mn_{50}Ni_{42}Sn_8$ Heusler alloy, Appl. Phys. Lett. **106**, 072405 (2015).

[24] G. D. Liu, J. L. Chen, Z. H. Liu, X. F. Dai, G. H. Wu, B. Zhang, and X. X. Zhang, Martensitic transformation and shape memory effect in a ferromagnetic shape memory alloy, Appl. Phys. Lett. **87**, 262504 (2005).

[25] See Supplemental Material at http://link.aps.org/supplemental/10.1103/PhysRevB.107.054405 for auxiliary information about XRD at room temperature, the Neel Arrhenius law, aging effects in the ZFC and FC protocol, and exchange bias at 2 K after FC at a −10 kOe field.

[26] T. Krenke, X. Moya, S. Aksoy, M. Acet, P. Entel, L. Manosa, A. Planes, Y. Elerman, A. Yucel, and E. F. Wassermann, Electronic aspects of the martensitic transition in Ni–Mn based Heusler alloys, J. Magn. Magn. Mater. **310**, 2788 (2007).

[27] K. Binder and A. P. Young, Spin glasses: Experimental facts, theoretical concepts, and open questions, Rev. Mod. Phys. **58**, 801 (1986).

[28] J. A. Mydosh, *Spin Glasses: An Experimental Introduction* (Taylor & Francis, London, 1993).

[29] D. Y. Cong, S. Roth, and Y. D. Wang, Superparamagnetism and superspin glass behaviors in multiferroic NiMn-based magnetic shape memory alloys, Phys. Status Solidi B **251**, 2126 (2014).

[30] D. Y. Cong, S. Roth, J. Liu, Q. Luo, M. Potschke, C. Hurrich, and L. Schultz, Superparamagnetic and superspin glass behaviors in the martensitic state of $Ni_{43.5}Co_{6.5}Mn_{39}Sn_{11}$ magnetic shape memory alloy, Appl. Phys. Lett. **96**, 112504 (2010).

[31] M. Thakur, M. Patra, S. Majumdar, and S. Giri, Coexistence of superparamagnetic and superspin glass behaviors in $Co_{50}Ni_{50}$ nanoparticles embedded in the amorphous $SiO_2$ host, J. Appl. Phys. **105**, 073905 (2009).

[32] E. Winkler, R. D. Zysler, M. V. Mansilla, D. Fiorani, D. Rinaldi, M. Vasilakaki, and K. N. Trohidou, Surface spin-glass freezing in interacting core–shell NiO nanoparticles, Nanotechnology **19**, 185702 (2008).

[33] N. Marcano, J. C. Gómez Sal, J. I. Espeso, L. Fernández Barquín, and C. Paulsen, Cluster-glass percolative scenario in Ce $Ni_{1-x}Cu_x$ studied by very low-temperature AC susceptibility and DC magnetization, Phys. Rev. B **76**, 224419 (2007).

[34] D. N. H. Nam, R. Mathieu, P. Nordblad, N. V. Khiem, and N. X. Phuc, Spin-glass dynamics of $La_{0.95}Sr_{0.05}CoO_3$, Phys. Rev. B **62**, 8989 (2000).

[35] M. Sasaki, P. E. Jonsson, H. Takayama, and H. Mamiya, Aging and memory effects in superparamagnets and superspin glasses, Phys. Rev. B **71**, 104405 (2005).

[36] S. Sahoo, O. Petracic, W. Kleemann, P. Nordblad, S. Cardoso, and P. P. Freitas, Aging and memory in a superspin glass, Phys. Rev. B **67**, 214422 (2003).

[37] S. Bedanta and W. Kleemann, Supermagnetism, J. Phys. D Appl. Phys. **42**, 013001 (2009).

[38] D. S. Fisher and D. A. Huse, Nonequilibrium dynamics of spin glasses, Phys. Rev. B **38**, 373 (1988).

[39] D. S. Fisher and D. A. Huse, Equilibrium behavior of the spin-glass ordered phase, Phys. Rev. B **38**, 386 (1988).

[40] R. B. Helmholdt and K. H. J. Buschow, Crystallographic and magnetic structure of $Ni_2MnSn$ and $NiMn_2Sn$, J. Less Common Met. **128**, 167 (1987).

[41] H. Luo, G. Liu, Z. Feng, Y. Li, L. Ma, G. Wu, X. Zhu, C. Jiang, and H. Xu, Effect of the main-group elements on the electronic structures and magnetic properties of Heusler alloys $Mn_2NiZ$ ($Z$ = In, Sn, Sb), J. Magn. Magn. Mater. **321**, 4063 (2009).

[42] S. Paul and S. Ghosh, First-principles prediction of shape memory behavior and ferrimagnetism in $Mn_2NiSn$, J. Phys. Condens. Matter **23**, 206003 (2011).